Acta Biomaterialia 195 (2025) 536–546

Contents lists available at ScienceDirect

Acta Biomaterialia

journal homepage: www.elsevier.com/locate/actbio

Short communication

Photoswitching protein-XTEN fusions as injectable optoacoustic probes

Yishu Huang [a,b,1], Mariia Stankevych [a,b,1], Vipul Gujrati [a,b], Uwe Klemm [a,b], Azeem Mohammed [a,b], David Wiesner [a], Mara Saccomano [c], Monica Tost [d], Annette Feuchtinger [d], Kanuj Mishra [a,b,*], Oliver Bruns [c], Arie Geerlof [e], Vasilis Ntziachristos [a,b], Andre C. Stiel [a,b,f,*]

[a] Institute of Biological and Medical Imaging, Bioengineering Center, Helmholtz Zentrum München, Neuherberg, Germany
[b] Chair of Biological Imaging, Central Institute for Translational Cancer Research (TranslaTUM), School of Medicine and Health & School of Computation, Information and Technology, Technical University of Munich, Munich, Germany
[c] Helmholtz Pioneer Campus, Helmholtz Zentrum München, Neuherberg, Germany
[d] Core Facility Pathology & Tissue Analytics, Helmholtz Zentrum München, Neuherberg, Germany
[e] Protein Expression and Purification Facility, Institute of Structural Biology, Helmholtz Center Munich for Environmental Health, Neuherberg, Germany
[f] Protein Engineering for Superresolution Microscopy Lab, University of Regensburg, Regensburg, Germany

ARTICLE INFO

Keywords:
Photo-/ optoacoustic
Injectable probe
XTEN
Photoswitching
Bacteriophytochromes
Imaging

ABSTRACT

Optoacoustic imaging (OAI) is a unique in vivo imaging technique combining deep tissue penetration with high resolution and molecular sensitivity. OAI relying on strong intrinsic contrast, such as blood hemoglobin, already shows its value in medical diagnostics. However, OAI sensitivity to current extrinsic contrast agents is insufficient and limits its role in detecting disease-related biomarkers. The recently introduced concept of photoswitching and temporal unmixing techniques for OAI allows detecting extrinsic contrast with high sensitivity, allowing the visualization of small populations of cells labeled with photoswitching proteins deep within the tissue. However, transgene modification might not be permitted in some cases, such as for diagnostic use. Therefore, it is desirable to leverage the concept of photoswitching OAI towards injectable formulations. Since photoswitchable synthetic dyes are mainly excited by blue wavelengths unsuited for imaging in tissue, we propose exploiting the addition of XTENs to photoswitching proteins towards yielding injectable agents. The addition of XTEN to a protein enhances its plasma half-life and bioavailability, thus allowing its use, for example, in targeted labeling approaches. In this pilot study, we show that intravenously injected near-infrared absorbing photoswitchable proteins, *Re*BphP-PCM, coupled to XTEN, allow highly sensitive optoacoustic visualization of a tumor xenograft in vivo. The sensitivity to XTENs-*Re*BphP-PCM determined by *ex vivo* analysis of labeled cells is one to two orders of magnitude beyond conventional synthetic dyes used currently in OAI. The enhanced sensitivity afforded by photoswitching OAI, in combination with the increased bioavailability and biocompatibility of XTENs-*Re*BphP-PCM, makes this fusion protein a promising tool for facilitating sensitive detection of biomarkers in OAI with a potential for future use in diagnostics.

Statement of significance: Optoacoustic imaging (OAI) is a unique in vivo imaging technique that combines deep tissue penetration with high resolution. OAI, which relies on intrinsic contrast, such as blood hemoglobin, could already be valuable in medical diagnostics. However, the use of extrinsic contrast agents to augment disease-related biomarkers in research and diagnostics suffers from very limited sensitivity of the generated contrast agent. We present an intravenously injected photoswitchable protein, *Re*BphP-PCM, coupled to XTEN, allowing highly sensitive OAI. The sensitivity is one to two orders of magnitude greater than that of conventional synthetic dyes used currently in OA imaging. The high sensitivity afforded by photoswitching together with the enhanced bioavailability and biocompatibility of the XTENs-*Re*BphP-PCM make this a standard agent for high-quality detection of OAI with potential for clinical use.

* Corresponding authors.
E-mail addresses: kanuj.mishra@tum.de (K. Mishra), andre.stiel@helmholtz-munich.de (A.C. Stiel).
[1] These authors contributed equally

https://doi.org/10.1016/j.actbio.2025.02.002
Received 29 May 2024; Received in revised form 20 January 2025; Accepted 3 February 2025
Available online 4 February 2025

1. Introduction

Optoacoustic imaging (OAI; also known as photoacoustic imaging) combines optical contrast with ultrasound resolution, enabling high-resolution real-time in vivo imaging well beyond the 1 mm penetration depth typical for optical methods [1,2]. OAI has been highly successful in clinical imaging [3] of psoriasis [4], metabolic function [5], Crohn's disease [6], collagen as a biomarker for muscular dystrophy [7], etc. This success extends to using OAI in theranostic research [8] and biomedical imaging of brain activity [9], metastases in sentinel lymph nodes [10], and so on. While all of these studies rely on endogenous absorbers, such as blood, melanin, or lipids, to generate contrast, the use of targeted exogenous contrast is more limited, with pre-clinical research mainly using synthetic agents or genetically encoded tools (reviewed in [11–14]). Notable examples include tracking melanogenic circulating tumor cells (CTCs) [15], macrophage migration [16], or progression of labeled tumors [17–19]. However, most exogenous agents struggle to outcompete the strong signal from endogenous absorbers, resulting in low detection sensitivity. To elaborate, conventional exogenous OAI agents, such as Indocyanine Green (ICG), IRDye800, or gold nanorods (GNR), are visualized with multispectral imaging and measured after spectral unmixing. However, the spectrums of these exogenous agents have peaks that overlap with the peaks of several confounders (oxy- and deoxy-hemoglobin, lipids, etc.). The mathematical solution (in its simplest case, a linear regression) informs on the presence and relative concentration of the agent in each voxel. However, this approach is confounded by spectral coloring, meaning that the light propagating through the tissue is affected by the various endogenous absorbers in its path, leading to the attenuation of the light to an unknown extent at each wavelength. In other words, the observed spectral signal is always a convolution of the agent in the voxel and the fluence at each wavelength at this position in the tissue. Hence, the lack of fluence information effectively limits the accuracy of spectral unmixing, especially at low agent concentrations. In contrast to conventional exogenous agents, the recent introduction of photoswitching proteins for OAI afforded a massive boost in detection sensitivity for targeted contrast [20,21]. Photoswitching creates a specific, known modulation of the agent's signal, which facilitates differentiation of its signal from the non-modulated background of endogenous absorbers (Fig. 1a) [21,22]. Hence, in contrast to spectral unmixing, only the temporal development of *one* wavelength is required, making the method more robust against the heterogeneous and unknown change of the incident light spectrum in tissue. For example, near-infrared absorbing photoswitchable Bacteriophytochromes (BphPs) used as transgene labels allow the detection of <1000 transgene labeled cancer cells in the mouse body using optoacoustic (OA) tomography [23,24], the multiplexed visualization of three labeled populations of T-lymphocytes in a live mouse [25], the use in a raster scanning OAI approach [26] or the combination with optogenetics in a transgene mouse [27]. While these advances in contrast from photoswitching transgenes boost the imaging capabilities of OAI for life sciences, similar solutions for targeted contrast in situations that do not permit transgene modification or for future diagnostic imaging applications are still lacking. Present works utilize synthetic dyes like ICG, fluorescein, or plasmonic nanoparticles [12,28], whereby only the first two are FDA-approved and the last is under scrutiny due to possible toxicity [29]. Synthetic photoswitching dyes, which would be required for photoswitching OAI, exist. However, they are predominantly photoswitched by wavelengths <700 nm [30–33], which are unfavorable for in-tissue imaging. Furthermore, despite some progress [34,35], the development of photoswitching synthetic dyes in the near-infrared (NIR) regime remains challenging due to the lower energies available for photoswitching. Workarounds like pairing upconverting nanoparticles with dyes absorbing well below 700 nm work, but this approach results in slow switching [36]. In photoswitching BphPs, which typically absorb around 700 nm, these limitations are overcome by chromophore photophysics that have been

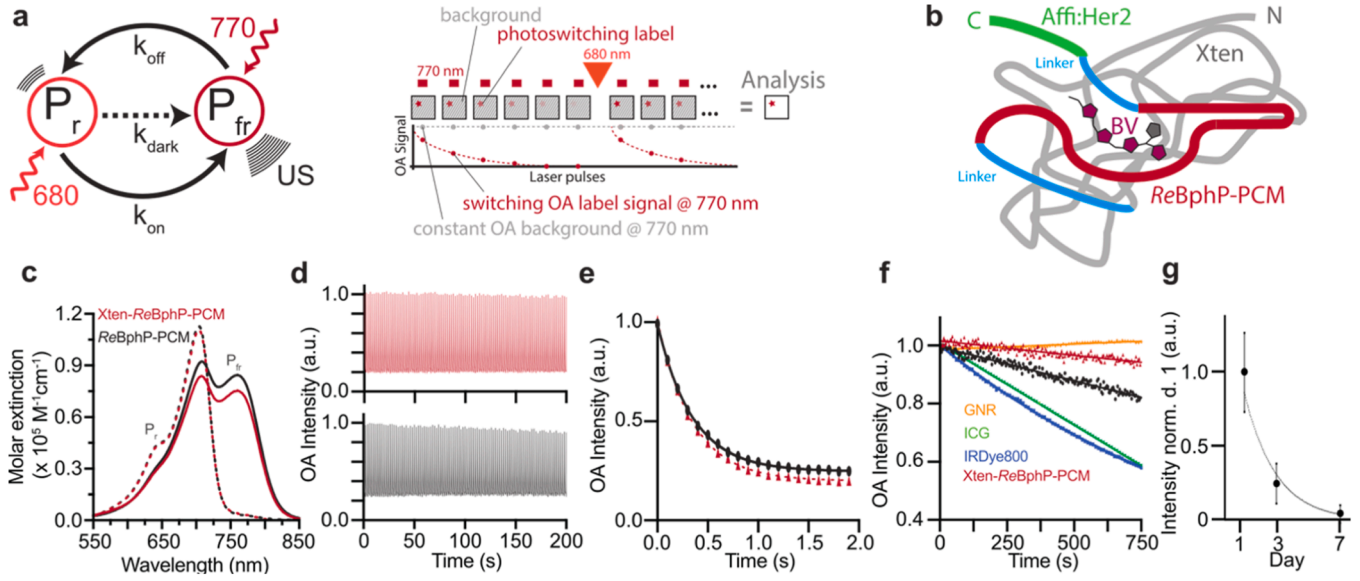

Fig. 1. a Left panel: Schematic illustrating the reversible photo-switching of bacteriophytochromes (BphPs) between the red (P_r) and far-red (P_{fr}) state after irradiation with 680 nm or 770 nm light. Right panel: The photo-switching of BphPs allows signals from labeled cells (indicated in red) to be differentiated from the non-modulated background of blood (indicated in grey). b Schematic showing XTEN (grey) attached to the N-terminus of Biliverdin (BV)-bound BphP (red). For targeting purposes, for example, an Affibody can be attached to the C-terminal (green). c Absorbance spectra of XTEN-*Re*BphP-PCM protein and its parent *Re*BphP-PCM protein at their equilibrium P_{fr} and photo-switched P_r state. The spectra are normalized to their Soret band (the full spectra can be found in Suppl. Fig. 2). d Normalized signal after multiple photo-switching cycles of both proteins. e A zoomed-in view of a single cycle from panel (d) shows the similarity of kinetics for both proteins. f Photofatigue of the two proteins compared with common optoacoustic imaging (OAI) agents requiring spectral unmixing for detection. The points indicate signals at the beginning of each switching cycle (20 pulses at 770 nm and 20 pulses at 680 nm) or a similar number of pulses at the wavelength of the absorbance peak for the non-switching agents. The illumination in the sample plane is expected to be homogenous ~3 mJ/cm^2. The concentrations of the different agents were around 3 μM. g In vivo plasma stability of XTEN-*Re*BphP-PCM. The data is represented as mean and standard deviation (N = 5) normalized to the intensity on day 1, single exponential decay is shown for orientation only. OA: optoacoustic.

elaborately tuned by the natural protein environment [37].

Here, we explore using the recently introduced photoswitching BphP protein *Re*BphP-PCM [25] as an administered exogenous agent for in vivo cancer imaging in mice. This approach could indicate the potential of conferring the superior OAI sensitivity afforded by photoswitching for diagnostics. Beyond that, such formulations provide a labeling option for highly sensitive target detection in research studies that do not allow transgene modifications. Recent works have shown that long unstructured polypeptide chains, called XTENs [38], exert a similar effect to PEGylation for synthetic molecules, allowing for longer plasma half-life and bioavailability. Recently, a first clinical trial on a treatment for hemophilia demonstrated the promise and clinical applicability of the XTEN concept [39]. Importantly, while XTENs have been used for SPECT/CT imaging when a protein for in vivo detection of apoptosis was coupled to a radionucleotide [40] or MRI when XTENS were coupled to gadolinium to detect lung cancer metastasis [41], the use of XTENs to confer the particular properties of protein-based contrast agents to imaging has not yet been shown. We demonstrate that fusion constructs of XTENs and photoswitching BphPs can be injected into mice, where they passively label tumors due to enhanced permeability and retention effect (EPR), enabling highly selective and sensitive OAI visualization for tumor marking. Moreover, combination with targeting moieties like Affibodies could allow for even more epitope-specific visualization of targets, such as cancer cells. Importantly, such constructs could be clinically approved presenting a path towards translating the superior sensitivity of photoswitching OAI to diagnostic applications.

2. Material and methods

2.1. Cloning

The bacterial expression vector pET-Duet1 containing the XTEN DNA sequence (coding for 896 amino acids including a 12 amino acid C-terminal flexible linker (SSSSGSSSSGGS)) in multiple cloning site two was ordered from GeneArt, Life Technologies, Regensburg, Germany. Then, for biliverdin synthesis, the heme oxygenase (HO) of Nostoc sp. was cloned into the first multiple cloning site of pET-Duet1 after Nco I/HindIII restriction digest and ligation. Finally, *Re*BphP-PCM DNA (including codons for the C-Terminal His_8-Tag) was amplified using polymerase chain reaction (PCR), restriction digested with BamH1/Xho I, and the fragments were cloned in frame at the 3` end of the XTEN sequence using the second multiple cloning site of the pET-Duet1 vector.

2.2. Cell culture

4T1 (ATCC, order nr. CRL2539) and HCC1954 cells (ATCC, order nr. CRL2338) were cultured in RPMI 1640. SKOV3 (Elabscience, order Nr. CL-0215) and MDA-MB468 cells (ATCC, order Nr. HTB 132) were maintained in McCoy 5A medium and DMEM, respectively. All media were supplemented with 10 % fetal bovine serum (Invitrogen, Massachusetts, USA), and antibiotics (penicillin (100 U/ml) and streptomycin (100 mg/ml)). HUVEC cells were cultivated in Endothelial Cell Growth Medium 2 (PromoCell, Heidelberg, Germany). All cells were incubated at 37 °C and 5 % CO_2 and passaged 2–3 times per week.

2.3. Conjugation of IRDye 800CW to Trastuzumab

IRDye® 800CW (LI-COR Biosciences, Lincoln, NE, USA) was conjugated to Trastuzumab (Herceptin®, Roche, Basel, Switzerland) at a dye-to-protein ratio (DOL) of 1:1 according to the manufacturer instructions. After the conjugation, unconjugated dye was removed by Zeba™ Spin Desalting Plates (Thermo Scientific, Massachusetts, USA). The final DOL and concentration of conjugated antibody were calculated according to the absorbance at 280 nm and 780 nm using a UV–VIS spectrophotometer (DeNovix, Wilmington, USA).

2.4. Bacterial expression and purification

The expression plasmid coding for photoswitchable XTEN-His_8 was transformed into *E. coli* BL21 (DE3) and the *E. coli* were cultured in Terrific Broth containing 100 μg/ml carbenicillin. The expression of XTEN-His_8 was induced by adding 0.5 mM isopropyl-thiogalactopyranoside (IPTG) after the *E. coli* reached an OD of approximately 2 at 600 nm. After induction, the cultures were incubated overnight at 20 °C. Cells from 1 l of culture media were harvested and resuspended in 60 ml lysis buffer (50 mM Tris–HCl, 300 mM NaCl, 20 mM imidazole, 10 mM $MgCl_2$, 10 μg/ml DNaseI, 1 mM AEBSF.HCl (4-benzenesulfonyl fluoride hydrochloride), 0.2 % (v/v) NP-40, 1 mg/ml lysozyme, 0.01 % (v/v) 1-thioglycerol, pH 8.0), and then sonicated. The lysates were clarified by centrifugation and filtration and the supernatant was applied to a 5 ml HiTrap chelating HP column (GE Healthcare, Illinois, USA), equilibrated with buffer A (50 mM Tris–HCl, 300 mM NaCl, 20 mM imidazole, 0.01 % (v/v) 1-thioglycerol, pH 8.0) using an Äkta Purifier (GE Healthcare, Illinois, USA). Bound proteins were eluted with a linear gradient of imidazole ranging from 20 to 300 mM and eluted fractions with a green color were pooled and dialyzed overnight at 4 °C against 1 l of 50 mM Tris–HCl, 300 mM NaCl, 0.01 % (v/v) 1-thioglycerol, pH 8.0). The dialyzed solution was concentrated using a centrifugal membrane concentrator and then diluted 6-fold with 20 mM Tris–HCl pH 7.5. This solution was applied to a 5 ml HiTrap Q HP column (GE Healthcare, Illinois, USA), equilibrated with 20 mM Tris–HCl, 50 mM NaCl, pH 7.5, and the bound proteins were eluted with a linear NaCl gradient ranging from 50 to 1000 mM. Fractions with a green color were pooled, concentrated as above to 1.0 ml, and applied to a Superose 6 10/300 GL column (GE Healthcare, Illinois, USA) equilibrated with 20 mM Tris–HCl, 150 mM NaCl, pH 7.5. Fractions with a green color were pooled and concentrated as abvove to 10 mL, then applied to a HiLoad® 26/600 Superdex® 200 pg column (GE Healthcare, Illinois, USA) equilibrated with phosphate-buffered saline (PBS) pH 7.4. Fractions with a green color were pooled, concentrated, and the right molecular weight of the constructs verified on 7 % SDS-PAGE. The purified protein was flash-frozen in liquid nitrogen in 0.5 ml aliquots and stored at −80 °C until further use.

2.5. Absorption and fluorescence spectroscopy

To collect absorption spectra, the proteins were measured with a Shimadzu UV-1800 spectrophotometer (Shimadzu Inc., Kyoto, Japan) using a 100 ml quartz cuvette with a 1 cm path length. To measure the ON (P_{fr}) and OFF (P_r) spectra of XTEN-*Re*BphP-PCM, photoswitching conducted out using 650/20 nm or 780/20 nm light-emitting diodes (Thorlabs) with a liquid light guide placed into the cuvette in the spectrophotometer. Fluorescence measurements were done at an excitation wavelength of 700 nm and an emission wavelength of 720 nm. The excitation and emission slits were set to 5 nm. For the fluorescence the sample solutions were diluted to have an absorbance equivalent to 0.1 at the excitation wavelength to avoid inner filter effects.

2.6. Photoacoustic signal generation efficiency (PGE)

PGE comparison was performed using phantoms (3 % intralipid, 2 % agarose) consisting of straws filled with either with XTEN-*Re*BphP-PCM or BrilliantBlueG at different concentrations. PGE was calculated by comparing the signal at peak wavelength after reconstruction.

2.7. In vitro viability assays

Flow cytometry analyses were performed to assess the viability and apoptosis of cells following treatment with XTEN-*Re*BphP-PCM at concentrations from 1 to 10^5pM for 72 h. Cells were analyzed using the BD FACSymphony™ A3 Cell Analyzer (BD, New Jersey, USA) after applying the FITC Annexin V/Dead Cell Apoptosis Kit (Invitrogen, Massachusetts,

USA), following the manufacturer's instructions.

Briefly, 4T1, SKOV3, and HUVEC cells were treated separately with XTEN-*Re*BphP-PCM in triplicates. The cells were incubated with XTEN-*Re*BphP-PCM concentrations selected based on the literature regarding XTEN toxicity [42]. After 72 h of incubation, adherent cells were trypsinized and combined with the floating dead cells in the media of the same culture flask. Cells were then washed, pelleted, resuspended in the manufacturer`s binding buffer, and stained with Annexin V-FITC and propidium iodide (PI) before analyzing.

Data was acquired using the BD FACSymphony™ A3 Cell Analyzer with the BD FACSDiva™ Software (BD Biosciences, Heidelberg, Germany), and subsequential analyses were conducted using the FlowJo 10.1.08 software (BD Biosciences, Heidelberg, Germany). Living cells were Annexin V^-/PI^-, apoptotic cells were Annexin V^+/PI^-, and dead cells were Annexin V^+/PI^+. With the numbers of live, apoptotic, and dead cells, cell viability could be calculated by expressing the sum of dead and apoptotic cells over total cells as a percentage. The results are presented as means ± SD.

2.8. SKOV3 labeled cells phantom and ex vivo measurements

SKOV3 cells were trypsinized and then stained separately with XTEN-*Re*BphP-PCM-Affi or IRDye800-Trastuzumab [43]. The SKOV3 cells were suspended in a staining solution containing 0.158 nmol of IRDye800-Trastuzumab antibodies per million cells. These antibody concentrations were selected to ensure complete saturation of the HER2 receptors, as the antibodies were 50-fold more than the receptors present. The staining times were optimized for optimal binding (3 h for XTEN-*Re*BphP-PCM-Affi and 1 h for IR800-Trastuzumab). Following staining, the cells were washed with PBS three times and imaged using a fluorescence microscope (DM2500, Leica, Wetzlar, Germany) equipped with Cy5.5 and IR800. Subsequently, phantoms were prepared by diluting the cells with varying volumes of 4 % alginate solution before loading the various concentrations of diluted cells into 580 μm catheter tubing. Afterward, the same catheter tubing filled with different concentrations of SKOV3 cells were implanted subcutaneously in the backs of euthanized Foxn1nu mice and imaged ex vivo using Multispectral Optoacoustic Tomography (MSOT, iThera Medical, Gemany; N = 3).

2.9. Confocal imaging

Chamber slides (Ibidi, Gräfelfing, Germany) were coated with Poly-D-Lysine (Gibco, New York, USA) according to the manufacturer's instructions. SKOV3 cells were seeded into the wells of the chamber slide one night before analysis. Cells were stained with XTEN-ReBphP-PCM-Affi or IR800-Trastuzumab. To assess the colocalization of XTEN-*Re*BphP-PCM-Affi with lysosomes, Lysotracker Green DND-26 (Life Technologies, Regensburg, Germany) was added for the final hour of incubation. After incubation, the cells were washed with PBS and stained with 7.5 μg/mL Hoechst solution to visualize nuclei. After removing the plastic chambers, the slides with the adherent cells were mounted using Vectashield antifade mounting medium and coverslips.

Images of SKOV3 labeled with XTEN-*Re*BphP-PCM-Affi or IRDye800-AB were acquired using an Axioscan 7 microscope-slide-scanner (Zeiss, Jena, Germany), utilizing 633 nm and 725 nm laser excitations for visualizing XTEN-*Re*BphP-PCM-Affi and IR800-Trastuzumab, respectively. To visualize the colocalization of XTEN-*Re*BphP-PCM-Affi and lysosomes, a STELLARIS 8 confocal microscope (Leica, Wetzlar, Germany) was utilized with 353 nm, 504 nm, and 660 nm laser excitations for Hoechst, Lysotracker and XTEN-*Re*BphP-PCM-Affi, respectively.

2.10. In vivo mouse work

All animal experiments were approved by the Government of Upper Bavaria and were carried out in accordance with the approved guidelines. For all MSOT imaging, mice were anesthetized using 2 % isoflurane in O_2. Anesthetized mice were placed in the MSOT holder using ultrasound gel and water as coupling media. After the termination of the experiments, all mice were sacrificed. For the toxicology study, C57BL/6 mice were randomly assigned into four groups ($n = 5$); group 1 was injected with PBS, and groups 2 to 4 were injected with 750 μg of XTEN-*Re*BphP-PCM. Groups 1 and 2 were sacrificed at 4 h after intravenous injection of PBS or XTEN-*Re*BphP-PCM, whereas groups 3 and 4 were sacrificed on Day 3 and Day 7, respectively. Blood samples were collected and analyzed for blood parameters. The organs (liver, kidney and spleen) were extracted and examined with OAI for the presence of photoswitchable XTEN-*Re*BphP-PCM proteins. For 4T1 xenografts, 0.8×10^6 cells in PBS were implanted subcutaneously in the back of immunodeficient CD1-Foxn1^{nu} (Foxn1^{nu}) mice (Charles River Laboratories, Boston, USA) 9 days before intravenous injection of PBS or XTEN-*Re*BphP-PCM. For SKOV3 xenografts, 1×10^6 cells in Matrigel (Corning, New York, USA) were implanted subcutaneously as described above. The mice were monitored until the tumors reached an approximate volume of 150 mm³. At this point, an intravenous injection of XTEN-*Re*BphP-PCM-Affi was administered. Imaging sessions were conducted before injection, as well as at 4 h, 24 h, and 48 h after the injection. Following imaging, the mice were sacrificed. Tumor xenograft volumes in cubic millimeters were calculated according to the ellipsoid formula $4/3\pi \times \text{length}/2 \times \text{width}/2 \times \text{width}/2$ [44].

2.11. MSOT setup and data acquisition for phantoms

Phantom data was acquired using a commercially available MSOT scanner (MSOT InVision 256-TF, iThera Medical GmbH, Munich, Germany). In brief, nanosecond pulsed light was generated by a tunable optical parametric oscillator (OPO) laser and delivered to the sample through a ring-type fiber bundle. Light absorbed by the sample generated an acoustic signal that propagated through the sample and was detected outside the sample by a cylindrically focused 256-element transducer. The transducer array had a central frequency of 5 MHz with a radius of curvature of 40 mm and an angular coverage of 270°. Acoustic signals were detected as time series pressure readouts at 2030 discrete time points at 40 MS/s (mega samples per second). The phantoms were prepared by mixing 3 % intralipid (Sigma-Aldrich, St. Louis, Missouri, USA) and 2 % agarose (Carl Roth, Karlsruhe, Germany) in a 50 ml sample tube to create phantoms of ~27 mm diameter. For the samples, straws were placed symmetrically ~5 mm off-center and filled with sample or 100 % sheep blood control (Thermo Scientific, Massachusetts, USA).

For the measurements in solution, purified XTEN-*Re*BphP-PCM, IRDye® 800CW, ICG (Sigma-Aldrich, St. Louis, Missouri, USA), or GNR (10 nm diameter, silica-coated; Sigma-Aldrich, St. Louis, Missouri, USA) were diluted to approximately similar optical densities at their peak wavelengths. For the molarities, see Supplemental Table 1. XTEN-*Re*BphP-PCM samples were imaged with an illumination protocol consisting of eleven 680 nm pulses and eleven 770 nm pulses repeated 50 times. IR800, ICG, and GNR were imaged between 680 and 960 nm in 5 nm steps and averaged 10 times to arrive to the same number of 450 laser pulses used for the photoswitching measurement. All data were recorded at 3 positions in the tube with 100 μm spacing between the positions.

2.12. MSOT setup and data acquisition for mice

Data from mice were collected using the MSOT scanner. Briefly, all mice were anesthetized with 2 % isoflurane in oxygen and positioned within the MSOT holder. Ultrasound gel (Parker Laboratories, Fairfield, New Jersey, USA) was applied to the intended scanning area as coupling media. The mice were scanned with a protocol comprising eleven 680 nm pulses and eleven 770 nm pulses repeated 50 times across the subcutaneous tumor region at 0.50 mm intervals. After the experiments, the mice were sacrificed and stored at −80 °C for cryosectioning [25].

2.13. MSOT data analysis

OA data were reconstructed using ViewMSOT 4.0.2.2 software (iThera Medical, Germany). Photoswitching OA data were reconstructed using a backprojection (version 3.8, 30 mm field of view, 100 μm resolution) and spectral OA data were reconstructed using model-based algorithms (version 4.0). All data were analyzed using Matlab 2018 and a custom library from iThera Medical (version 717 or 723). Rigid affine-based movement correction [45] and non-rigid diffusion-based movement correction [46] were consecutively performed on all time-series frames. Fluence correction was performed by exponential models [47], based on each pixel depth, estimated as the minimum distance from each point to the manually segmented sample border. The coefficients are based on measurements of a homogeneous blood-intralipid phantom (2 % intralipid, 5 % blood, 5 % agar) with 27 mm diameter repeated 3 times on 3 different days and averaged for the fluence correction model. The model was discretized in 2 mm concentric rings.

Reconstructed OA signals per pulse were grouped based on the known light schedule, yielding continuous image time series for 770 and 680 nm illumination, respectively. The time series represent a succession of switching cycles, each with a certain number of pulses (see text for details). Only the image series recorded with 770 nm illumination was used for further processing. For each pixel in the image time series, extreme outliers (i.e. time points with signals 5 times larger than standard deviations of the whole time series) were replaced by the mean value for the given pulse from all other cycles of the pixel. Data was analyzed to isolate pixels that show a repetitive cycling in signal intensities from high signal (ON) to low signal (OFF), indicating the presence of photoswitching proteins. The metrics indicating photoswitching were computed: Fourier transform, exponential fit and differential in signal. In detail, fast Fourier transform was performed on the normalized (max to 1) signals of the time series and the result at the expected frequency component and its harmonics were summed (referred to as the FFT value). Separately, as predictors for the machine learning (ML)-based classification, the expected frequency component, the sum of its harmonics, and the sum of all other frequencies were calculated (referred to as Fourier analysis values). Based on the mean cycle of the time series, the exponential OFF-switching behavior was probed by fitting the mean cycle as "$a + b\ \exp(-kx)$". The fit value k served as an estimation of switching kinetics. The quality of fit was described by an adjusted R-square value. The difference between the ON and OFF state (differential) was taken to be the difference between the beginning and the end of the exponential fit of this mean trajectory.

For ML-based analysis, the following features were used: (a) For all pixels: the laser energy at 770 nm together with its standard deviation based on diode readout. (b) On a per-pixel basis: i) depth from sample edge; ii) mean and standard deviation of the OA intensity trajectory; iii) maximal and minimal signal values, stated as the difference between maximum and minimum signal values; iv) sum of negative values of the OA intensity trajectory; v) Fourier analysis values (see above); vi) differential of the mean cycle; vii) deviation from expected decay – normal and reversed, calculated as absolute values of difference between real mean cycle and expected trajectory; viii) kinetics of exponential fit (normal and reversed); ix) R^2 of exponential fit (normal and reversed; x) a number of cycle analysis values: mean and standard deviation of the first and last value for each cycle as well as the number of cycles where the maximum of the cycle is the first pulse and the minimum is the last pulse. Based on the above features, PCA pre-defined (see below) combinational weights were applied, turning the 23 values into 8 combined predictors used in the final binary classification model. For each point, the 8 combined predictors were classified by a pre-trained (see below) random forest-based model. A per-pixel classification was used with pixels classified as switching or non-switching together with a confidence score [48]. PCA combinational weights were defined, and the classification model was built based on the following datasets: i) set of blood-intralipid phantoms (2 % intralipid, 5 % blood, 5 % agar) with straws of *Re*BphP-PCM solutions of different concentrations (OD_{770} 0.1, 0.05, 0.025) measured with different laser energies of the system (67, 59 and 45 mJ before coupling into the fiber); ii) 2 scans of a mouse without any agents, i.e. with no switching signals present with 2 different levels of laser energy (93 and 63 mJ); iii) subcutaneous implants of Matrigel containing bacteria expressed *Re*BphP-PCM at 2 different concentrations (57,000 cells/μl and 143,000 cells/μl); iv) mouse with 4T1 tumor, expressing *Re*BphP-PCM, scanned on several days during its growth. The datasets were annotated as switching and non-switching regions based on phantom and straw diameters or manually selected mouse borders and tumor borders according to histology results. Datasets were randomly divided so that 70 % and 30 % of the data were used for the training and validation processes, respectively, to establish the final classification model.

An anatomy image was made by taking the average of the co-registered images of the first pulse for the first 10 cycles. To assess the success of the different methods in a comparable fashion, the positive predictive value was used (true-positive / (true-positive + false-positive)). For this, the true- and false-positive rates were calculated and normalized to the respective regions-of-interest of the sample straw (true) and the phantom and control straw (false). Results for the three positions along the tube were averaged.

2.14. Serum stability

To gain insights into the stability and behavior of XTEN-*Re*BphP-PCM under physiological conditions, the XTEN-*Re*BphP-PCM were analyzed both in vitro and in vivo.

In vitro: To investigate the behavior of XTEN-*Re*BphP-PCM and *Re*BphP-PCM in plasma, 12.5 μg of each protein was incubated in mouse plasma (50 % final concentration) in PBS supplemented with NaN_3 (10 mM final concentration). The incubation was performed at 37 °C for varying 0, 1, or 7 days. Subsequently, the XTEN-*Re*BphP-PCM and *Re*BphP-PCM samples were diluted 1:200 and subjected to 7 % SDS PAGE and 10 % SDS PAGE, respectively, to separate the proteins based on their molecular weights. A Western blot analysis was conducted using mouse anti-His Tag antibodies to specifically detect the presence of the His-tagged XTEN-*Re*BphP-PCM and ReBphP-PCM.

In vivo: 10 μl of plasma was collected from each mouse that received an injection of 0.75 mg of XTEN-ReBphP-PCM (N = 5). The individual plasma samples were pooled. Subsequently, 5 μl of the pooled plasma sample was diluted with 15 μl of PBS and subjected to 7 % SDS PAGE. Following electrophoresis, a Western blot was performed to detect XTEN-*Re*BphP-PCM using mouse anti-His Tag antibodies.

2.15. Blood hematology and biochemistry analyses

C57BL/6 mice were randomly divided into 4 groups (5 mice per group). The control group (Group 1) was intravenously injected with 100 μl of PBS buffer, and the other 3 groups (groups 2 to 4) were intravenously injected with 750 μg of XTEN-*Re*BphP-PCM in 100 μl PBS. The same injections were repeated every week for the next 3 weeks. After each injection, blood was sampled from groups 1 and 2 on day 1 after the injection. Blood was sampled from groups 3 and 4 on day 3 and day 7 after injection, respectively. Whole blood samples were collected in EDTA tubes for full blood count analysis. For assessing clinical chemistry parameters, whole blood was collected in Li-heparin tubes and centrifuged at 5000 g for 10 mins at room temperature to collect plasma. The analyses were conducted using the Hitachi 917 Clinical Chemistry Analyzer (Roche, Germany). The mice were sacrificed 9 days after the last injection.

2.16. Statistical analysis

Results from in vitro viability assays and mouse blood analyses were

presented as means ± standard deviation (SD). Statistical comparison between groups was conducted using Wilcoxon-Mann-Whitney-Tests using GraphPad Prism 6.01 software (GraphPad Software Inc., California, USA). P-values less than 0.05 were defined as statistically significant.

For the imaging data, the calculation of mean and SD for a given number of samples (N indicated in the figure, text, or Supplementary Table 1) compares the unmixing result of the tumor ROI to the mouse ROI of a given mouse (i.e. the outline of the complete mouse). The same rationale is used for the comparison of the raw unmixing metrics (differential, rsqr or fft). Tumor ROIs are manually chosen based on the raw signals after excitation at 770 nm. The manual choice of the ROIs is executed rather graciously. In the case of suboptimal ROI placement, this results in an under- rather than an overestimation of the numerical results.

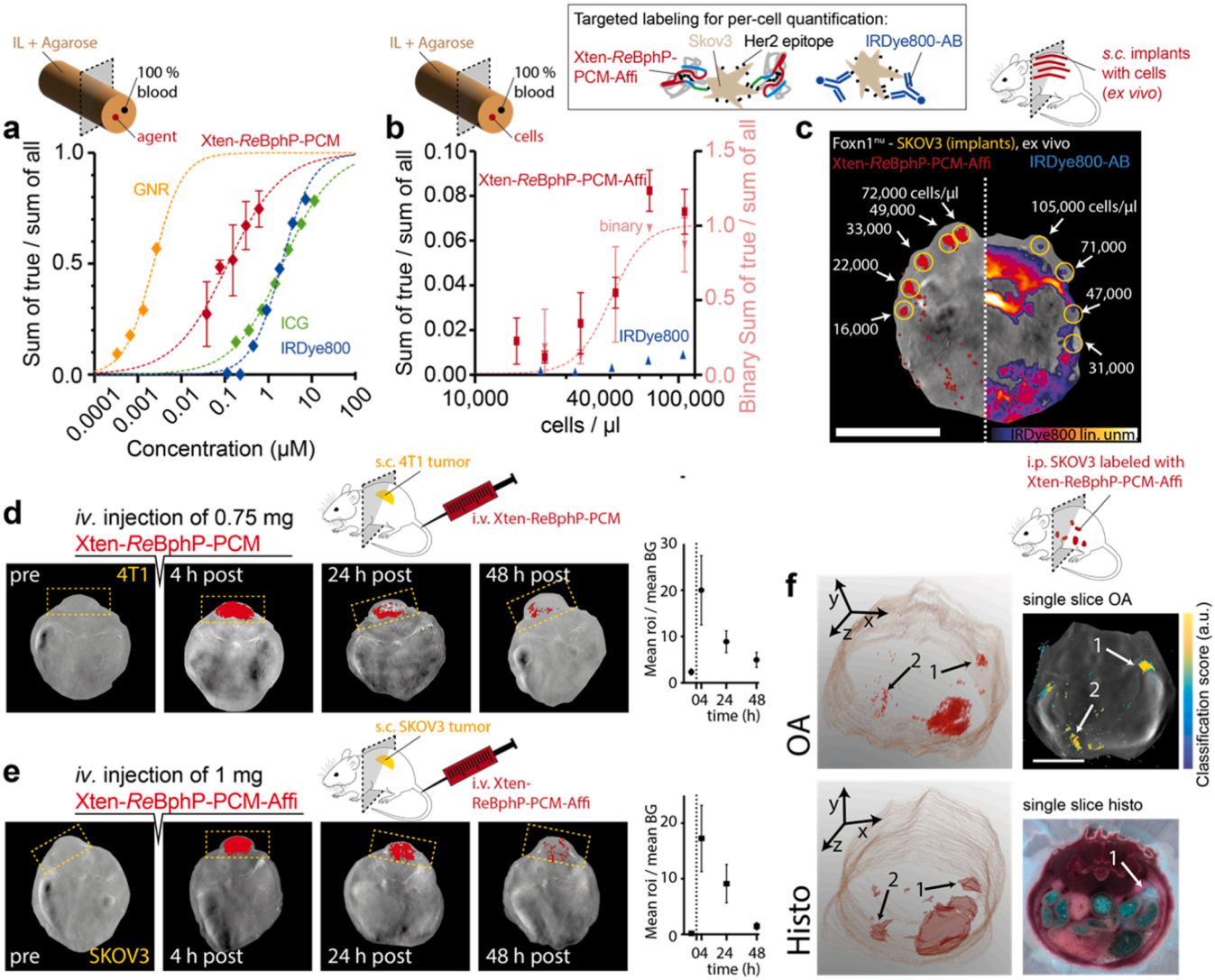

Fig. 2. a Detection of the different agents dissolved at varying concentrations in tubing embedded in tissue-mimicking phantoms. Comparison is performed by comparing the mean pixel values of only the sample straw with the mean pixel values of the complete phantom including the straw. True and false signals are defined based on the known ground truth of the phantom composition. The graph with the respective concentration in weight/volume is shown in Suppl. Figure 7. Details on the metric can be found in Suppl. Figure 4. Phantom imaging as depicted, tomographic imaging plane in gray. b Tissue-mimicking phantom for comparing SKOV3 cells labeled by HER2-Affi targeted XTEN-*Re*BphP-PCM or HER2 (Trastuzumab)-targeted antibody with IRDye800CW. Analysis as in a. For XTEN-*Re*BphP-PCM-Affi, the result for the unmixing metrics is shown based on a binary decision (agent and no agents) as well as based on the underlying continuous confidence score. Inset: Labeling strategies for SKOV3 cells. c *Ex vivo* in tissue comparisons of different numbers of implanted SKOV3 cells labeled as in the experiment shown in b. Note that the XTEN-*Re*BphP-PCM-Affi-labeled SKOV3 cells are shown as a binary representation, while the IRDye800CW-AB labeled cells show a continuous scale to allow visualization of the tubing above the strong background. d Representative optoacoustic image showing in vivo imaging of mice bearing subcutaneous 4T1 tumor models injected with XTEN-*Re*BphP-PCM. Right: Mean pixels in tumor ROI to mean pixels in mouse body obtained using binary machine learning (ML) analysis. Means and standard deviations are given for N = 3 mice. e Similar images of SKOV3 bearing mice injected with HER2-Affi targeted XTEN-*Re*BphP-PCM. Right: as in d for N = 4 mice. f Intraperitoneal implantation of XTEN-*Re*BphP-PCM-Affi-labeled SKOV3 cells. Left side: volumetric representations of switching unmixed (classification) in vivo OAI data (top) and segmented histology (bottom) both shown with a binary color scheme. Right side: Selected slice in histology and corresponding unmixed MSOT showing smaller tumor aggregates indicated by arrows (1 and 2) (note that resolution along the mouse axis strongly differs between MSOT and histology). The histology image is an overlay of brightfield and Cy5 channel. All scalebars are 10 mm. Abbreviations: IL = intralipid, s.c. = subcutaneous, i.v. = intravenous, OA = optoacoustic.

3. Results

3.1. Expression and photophysical characteristics of XTEN-ReBphP-PCM

We fused an 864 amino acid long (~80 kDa) XTEN [38] via a 12 amino acid linker to the N terminus of *Re*BphP-PCM[21] (Fig. 1b and Suppl. Fig. 1). After expression in *E. coli*, the construct could be readily purified using affinity and size exclusion chromatography to apparent purity (Suppl. Fig. 2), yielding ~4 mg of protein per liter of culture media. Lyophilized protein could be stored at −20 °C for >100 days without affecting the proteins' function or photoswitching ability (Suppl. Fig. 2e). XTEN-*Re*BphP-PCM showed the same absorbance characteristics as the parent *Re*BphP-PCM. Both proteins showed the characteristic Bathy-BphP spectrum with a far-red peak equilibrium state (P_{fr}) having absorption maxima at 760 and 708 nm (Fig. 1c). Illumination at the 760 nm peak of the protein allowed photoswitching to the red peak state (P_r), which showed a single peak at 703 nm. Illumination of the protein in this peak allowed the back-transition to the P_{fr} state. The absorption ratio of 280 nm and a wavelength corresponding to the Soret peak was almost similar for XTEN-*Re*BphP-PCM and its parent *Re*BphP-PCM, suggesting no detrimental influences of the XTEN on the chromophorylation of BphP (Suppl. Figure 3). The negligible contribution of the XTEN to the absorbance at 280 nm was due to its lack of aromatic amino acids. The kinetics and reversibility of the photoswitching were also virtually unchanged (Fig. 1d and 1e), suggesting that XTEN exerted no influence on the mobile PHY tongue of the BphP, which is relevant for the photoswitching behavior. The PGE at 770 nm referenced against Brilliant Blue G was similar for XTEN-*Re*BphP-PCM (1.14 ± 0.03) and *Re*BphP-PCM (1.12 ± 0.02). This suggests that the extensive disorganized polypeptide regions of the XTEN surrounding the *Re*BphP-PCM did not significantly influence the Grüneisen parameter for the OA signal generation. Finally, the photo-fatigue of XTEN--*Re*BphP-PCM was considerably lower than its parent *Re*BphP-PCM (Fig. 1f). This could be attributed to the XTEN potentially shielding the chromophore, reducing access to the surrounding solvent and hence decreasing photo-fatigue reactions [49] due to the presence of less molecular oxygen. The XTEN tail resulted in an extension of XTEN--*Re*BphP-PCM's stability in serum by several days compared *Re*BphP-PCM, as indicated by in vitro experiments examining these proteins in mouse plasma (Suppl. Fig 4). This is in line with previous studies that assessed XTEN's stability in serum, which showed the presence of the proteins for >7 days [50,51].

3.2. Benchmarking of XTEN-ReBphP-PCM performance in phantoms to assess its potential as an agent for OAI

The ability of agents to photoswitch enabled a dramatic increase in OAI detection sensitivity to them. We demonstrated this by comparing the detection of purified XTEN-*Re*BphP-PCM against well-established OAI contrast agents ICG [52,53], IRDye800CW (IRDye800) [54] and GNR (10 nm diameter, silica-coated) [55], with the former two being the contrast agents of choice for translational OAI. We measured tubes of contrast agents at different molar concentrations or a confounder tube containing whole blood in tissue-mimicking phantoms using an OA multispectral tomography (MSOT) device. A state-of-the-art linear regression unmixing approach was applied to multispectral data to unmix conventional contrast agents based on their spectral signatures (Suppl. Table 1). In contrast, the "temporal" signature of the photo-switching XTEN-*Re*BphP-PCM protein was acquired by recording a series of images at alternating wavelengths driving the photo-switching (11 pulses at 680 nm and 11 pulses at 770 nm for 20 cycles) and analyzed using an ML-based model [25] trained to identify the photo-switching behavior based on the intrinsic metrics of the varying signal over time, i.e., the signature in frequency space, the exponential decay behavior of the signals and the difference between the signal intensity at the beginning and end of a switching cycle [56] (Suppl. Table 1). A similar number of laser pulses was used to keep measurements of conventional contrast agents and photoswitching agents comparable, resulting in a 10x averaging of the recorded spectra for the "spectral" approach. The analysis shows that detection of XTEN-*Re*BphP-PCM is possible at molar concentrations almost 2-fold lower than the organic dyes, but only at 1 to 2-fold higher than GNR (Fig. 2a and Suppl. Figure 5 and 6; see Suppl. Figure 7 for a comparison based on the agents' concentrations in weight/volume). XTEN--*Re*BphP-PCM detection range between GNR and the organic dyes is in line with earlier results – e.g., see the comparison of noise equivalent concentrations in Yao et al. [57]. Beyond the detection sensitivity, a comparison of photo-fatigue characteristics showed XTEN-*Re*BphP-PCM is superior to ICG or IRDye800 (Fig. 1f). This characteristic will allow prolonged longitudinal measurements with repeated measurements while maintaining high sensitivity. Although visualization in live tissue is dependent on how much of the contrast agent can be targeted to the cells or tissue of interest (bioavailability), the photophysical capabilities of photoswitching BphPs and the reduced metabolic clearance rate granted by the XTEN conjugation XTEN-*Re*BphP-PCM make a promising agent.

3.3. Benchmarking of sensitivity of XTEN-ReBphP-PCM based on labeled cells

Next, we aimed to quantify the increased sensitivity to XTEN-*Re*BphP-PCM-labeled cells compared to cells labeled with a well-established OAI agent that requires conventional spectral unmixing. To achieve this, we expressed XTEN-*Re*BphP-PCM with a C-terminal affibody [58] targeted against the HER2 epitope (see inset between Fig. 2b and c). Affibodies are available for several disease-related epitopes [59] and, hence, can serve as an effective way to target the XTEN-*Re*BphP-PCM label. SKOV3 cells were cultivated, split into two identical batches and labeled either with the XTEN-*Re*BphP-PCM-Affi construct or a conventional clinically-approved and widely-used [60] HER2 antibody (Trastuzumab [61]) conjugated to IRDye800CW (IRDye800-AB). Several concentrations of the XTEN-*Re*BphP-PCM-Affi- or IRDye800-AB-labeled cells were measured in the same tissue-mimicking phantoms (Fig. 2b, Suppl. Figure 8). The measurements clearly show the advantage of using the photoswitching agent, XTEN-*Re*BphP-PCM-Affi, which is less affected by background, unlike IRDye800-AB. To explore this sensitivity quantitively in a tissue context, various concentrations of similarly labeled cells were loaded in 580 µm catheter tubing and implanted subcutaneously in the back of sacrificed $Foxn^{1nu}$ mice for imaging using MSOT (N = 3). After linear spectral unmixing was carried out on IRDye800-AB, only the tube with the higher concentration of cells were clearly visible (105.000 – 47.000 cells/µl). Detection of IRDye800-AB was made more challenging due to the strong false-positive signals arising primarily from the kidney region, likely due to spectral coloring caused by the high vascularization that complicated accurate spectral unmixing (Fig. 2c and Suppl Figure 9). In contrast, XTEN-*Re*BphP-PCM-Affi tubes with as little as 16,000 cells/µl were visible with negligible background. Hence, theoretically, the lowest detectable cell concentration amounts to ~200 cells in an imaging volume (cube with 200 µm sides, roughly the resolution of the device). Given that a single SKOV3 cell has approximately ~$1.38\,10^6$ HER2 epitopes [43], we estimated that 0.0023 fmol of XTEN--*Re*BphP-PCM per cell yielded a protein concentration of ~37 nM at 16,000 cells/µl, matching reasonably well with the detection sensitivity obtained in phantoms. The remaining discrepancy to the in-solution experiment might stem from the cell experiment being a convolution of several effects: the targeting to the HER2 epitopes by the Affibody and Antibody, respectively; the primary label signal; and the influence of the conjugation on the IRDye800-AB signal. In this context, we also examined whether the rather unstructured and bulky XTEN-*Re*BphP-PCM (~150 kDa) might hinder affibody-mediated targeting. Confocal microscopy imaging of XTEN-*Re*BphP-PCM-Affi using the low but

detectable fluorescence of *Re*BphP-PCM showed a similar membrane distribution as IRDye800-AB which is consistent with literature [58]. The levels of internalization are comparable to other uses of the HER2 Affibody [62] (Suppl. Figure 10). The internalization is likely related to a final localization of the agents in lysosomes. We confirmed XTEN--*Re*BphP-PCM-Affi colocalization with lysosomes by confocal microscopy (Suppl. Figure 11). Overall, these results suggest that affibody-based targeting can be a viable road for this type of photoswitching probe in general.

3.4. Biosafety and considerations for the in vivo use of XTEN-ReBphP-PCM

We determined that systemic application of XTEN-*Re*BphP-PCM by intravenous injection has no detrimental effect on mice. This finding fulfills the prerequisite to widespread application in other animal models and is an important first step toward translation to diagnostics. First, we tested the application of XTEN-ReBphP-PCM to SKOV3, 4T1, and HUVEC cells and assessed cell viability (Annexin V) and apoptosis (Propidium iodide) after the addition of 1 pM to 0.1 μM final concentration of XTEN-ReBphP-PCM (Suppl. Figure 12). Our results indicated no negative effects across all cell lines and doses. Next, we injected 0.75 mg of purified XTEN-*Re*BphP-PCM in C57BL/6 mice and sacrificed them at 4 h, 3 d, and 7 d post-injection (N = 4 per group). Despite a rather large amount of XTEN-*Re*BphP-PCM administered, no hematological parameters were significantly different when compared to the control group injected with phosphate buffer (PBS), suggesting that XTEN-*Re*BphP-PCM exerted no detrimental effects on vital organ functions or had immunogenic influence (Suppl. Figure 13–15). To assess the effect of repeated injections as might happen in a longitudinal imaging study, we injected mice (N = 2) with 0.75 mg of XTEN-ReBphP-PCM and repeated the same injection every week for the next 3 weeks. Both animals showed no pathological alterations in their livers, hearts, or lungs (Suppl. Figure 20). The blood analysis revealed slight reductions in red blood count (8.01 to 8.85×10^6/μL), hemoglobin (11.8 to 13.1 g/dL), and hematocrit (36.5 to 40.4 %) in the XTEN-*Re*BphP-PCM-injected mice (Suppl. Figure 16–19), which remained within clinically acceptable limits and did not indicate pathological damage. The mild changes were consistent with pathological assessment of the spleens, which indicated a mild increase of hematopoiesis and pale lymphoid follicles with a mild starry sky appearance, suggesting a stress response rather than toxicity (Suppl. Figure 20). One of the XTEN-*Re*BphP-PCM-injected mice presented with a mild pathological alteration of the kidney, while the other mouse showed tubular basophilia with no fibrotic or inflammatory alterations (Suppl. Figure 20). The latter mouse also had abnormal blood chemistry results, including low creatinine (0.153 mg/dL), high iron (94 μg/dL), elevated lactate (9.12 mmol/L), and increased lactate dehydrogenase activity (215.1 U/L), suggesting mild renal injury. Since these are mild regenerative changes that had no major impact on organ function, a toxic effect of the XTEN injection seems unlikely (Suppl. Figure 20). Moreover, we confirmed that adding an XTEN-tail to *Re*BphP-PCM lengthens its plasma-half life. I*n vitro* experiments showed that XTEN-*Re*BphP-PCM could be detected to day seven at least. In contrast, the protein without the XTEN shielding was undetectable after the first day. This indicates that XTEN-shielded XTEN-*Re*BphP-PCM and bestowed good plasma stability (Suppl. Figure 4a and b). In a similar way, we checked blood samples from mice (N = 5 pooled) injected with 0.75 mg of XTEN-*Re*BphP-PCM on days 1, 3, and 7 after injection. The XTEN-*Re*BphP-PCM protein could clearly be detected on day 1 but only faintly on day 3 and was not detectable on day 7 (Fig. 1g and Suppl. Figure 4c). This is in line with previous studies of showing a half-life of 30 h for XTEN constructs [63,64]. As XTEN-*Re*BphP-PCM has a high stability in plasma, the loss of the protein after 7 days is not due to degradation, but rather its clearance from the bloodstream and dilution. This is supported by the enrichment of XTEN-*Re*BphP-PCM in the tumor region after injection (see below).

3.5. Demonstration of XTEN-ReBphP-PCM and XTEN-ReBphP-PCM-Affi in vivo capabilities using OAI

We show the ability of XTEN-*Re*BphP-PCM to enable visualization of subcutaneous tumor xenografts in mice due to its prolonged retention in the tumor vasculature through the enhanced permeability and retention (EPR) effect. We intravenously injected 0.75 mg of XTEN-*Re*BphP-PCM in Foxn1^{nu} mice bearing subcutaneous 4T1 mouse breast cancer tumors (N = 3, Fig. 2d and Suppl. Figure 21). An overview of all mouse experiments, including implantation, tumor sizes, injections, and imaging conditions, can be found in Suppl. Table 1. The mice were scanned with MSOT, prior to injection and at 4, 24, and 48 h post-injection, using illumination alternating between 680 and 770 nm for inducing photoswitching at defined intervals for subsequent analysis as described above. While all pre-injection scans were devoid of signal patterns characteristic of photoswitching, we could detect the signal patterns indicating photoswitching in all cases 4 h after injection of XTEN-*Re*BphP-PCM in the tumor, and also in other organs, including the liver and kidneys. After 24 h had passed after injection, the presence of photoswitching was largely detected in the tumor. A control Foxn1^{nu} mouse (N = 1) devoid of a tumor showed only residual signals from XTEN-*Re*BphP-PCM in the spleen, liver, and kidneys (Suppl. Figure 22). To better illustrate the organ-specific localization of XTEN-ReBphP-PCM and its fast clearance, we injected the probe into C57Bl6 J mice without tumors before extracting the spleens, livers, and kidneys after 4 h or 72 h for assessment using MSOT (N = 2 × 5). While the 4 h timepoint showed clear signals from XTEN-ReBphP-PCM in all organs, no signal was detectable in the excised organs after 72 h (Suppl. Figure 23). Furthermore, we also explored mice growing a human breast cancer cell line (HCC1954), intravenously injected with 0.75 mg or 1.5 mg XTEN-*Re*BphP-PCM (Suppl. Figure 24 and 25). While the 0.75 mg dose predominantly resulted in signals at 4 h (N = 2) post-injection, the 1.5 mg dose resulted in visible signals at 4 and 24 h (N = 2) post-injection. XTEN-*Re*BphP-PCM-Affi could also be successfully detected in a SKOV3 mouse tumor model after intravenous injection (N = 2 × 4, Fig. 2e and Suppl. Figure 26 and 27).

To roughly estimate the cell number that can be well visualized in vivo, we used the targeted XTEN-*Re*BphP-PCM-Affi described earlier in the context of the *ex vivo* cell-based sensitivity quantification. We implanted SKOV3 cells labeled with XTEN-*Re*BphP-PCM-Affi intraperitoneally. After implantation, the cells were deposited in several clusters, allowing us to assess sites with different cell numbers and positions. We compared the unmixed photoswitching OA images with histological assessment to validate the detection of small, distributed tumor sites up to 4 mm deep in the mouse body. We found that approximately 100,000 cells/μl in smaller volumes 1–3 mm^3, corresponding to ~2000 cells in a $250\times250\times250$ μm^3 imaging voxel (Fig. 2f and Suppl. Figure 28 and 29) could be detected, showing high detection sensitivity near the resolution limits of the device.

4. Discussion

OAI is highly promising for clinical applications covering cancer detection, dermatology, vascular disease assessment, and beyond [65]. The advent of incorporating OAI into endoscopes has enabled scanning of the gastrointestinal tract that was previously beyond the depth limits (1 to 2 cm of tissue) of optoacoustic modalities when measuring from the skin surface [66]. Additionally, clinical OAI of the human brain has been demonstrated, though primarily limited to the cortex and in patients who had undergone a hemicraniectomy [67]. Overall, the low economic footprint comparable to MRI or PET and non-invasive nature of OAI make it a highly promising tool for routine diagnostics. Presently, most clinical applications using OAI rely on intrinsic blood contrast, with only a few using FDA-approved exogenous agents to highlight structures of interest, for example, lymph nodes [10] or microvasculature [68]. Current approaches are either limited by the low sensitivity of OAI

devices to conventional dyes designed for fluorescent applications or the poor biocompatibility to other agents (e.g. nanoparticles)[45], limiting OAI's widespread translation for diagnostic testing. This limitation could be overcome by using photoswitching proteins shielded by XTEN, which combine high biocompatibility (only modest stress responses after repeated administration) with photoswitching that enables enhanced detection by OAI modalities. We showed that XTEN-ReBphP-PCM could label subcutaneous tumors with at least one order of magnitude less material (10^{-2} μmol) compared to organic dyes, such as ICG [69–71] or IR800 [72] (typically 10^{0}-10^{-1} μmol). While noble metal nanoparticles require lower amounts of injected material (10^{-4}–10^{-6} μmol) [73–75], their biocompatibility remains a significant concern [29]. In contrast, XTEN-ReBphP-PCM has been shown here to exert no detrimental effects on mice. As synthetic dyes have considerably lower molecular weights compared to XTEN-ReBphP-PCM, it is challenging to relate detection to the "amount" of injected agent solely based on the weight or volume of the agents (see also differences between Fig. 2a and Suppl. Figure 7). Hence, we compared agents based on the number of detected cells detected after optimal labeling and showed that XTEN-ReBphP-PCM could be detected with higher sensitivity and precision (true detected pixel vs. all detected pixels) than the established agent IRDye800 (Fig. 2b and c). The likely reason for this improvement is that photoswitching agents are not detected via spectral unmixing and are, therefore, unaffected by spectral coloring, unlike all other agents. The photoswitching capability not only enables the higher detection sensitivity shown here but also suggests providing more reliable results when imaging heterogenous and highly vascularized tissues where spectral coloring is especially strong. Moreover, since photoswitching only requires 2 excitation wavelengths instead of multiple wavelengths for spectral agent, future diagnostic instruments could be equipped with fixed wavelength pulsed laser diodes [76,77] instead of a tunable source, significantly reducing the price of such devices. PASylation [78] based on a similar concept, hints at the potential of XTEN-shielded photoswitching proteins to be clinically translated. PASylation has already shown promising results in improving the pharmacokinetics of protein-therapeutics [79]. Early applications of PASylation combined with positron emission tomography (PET) imaging in clinical settings [80] demonstrated the feasibility of protein-based approaches for extending half-life. However, unlike these PASylated applications using PET, our photoswitching protein agents offer a fully biological label, without requiring radioactive labels and complex detection infrastructure. Additionally, lyophilized *Re*BphP-PCM-XTEN can be stored at room temperature for extended periods, and even longer at −20 °C, allowing easy shipment and handling. Beyond the translational potential of XTEN-shielded photoswitching protein agents, their high detection sensitivity is also valuable in research applications where transgene labeling is challenging, such as the imaging of primary immune cells [16]. In summary, XTEN-shielded photoswitching proteins, in conjunction with OAI, can deliver affordable and highly sensitive detection tools for research and future clinical diagnostics.

CRediT authorship contribution statement

Yishu Huang: Writing – review & editing, Writing – original draft, Investigation. **Mariia Stankevych:** Investigation. **Vipul Gujrati:** Writing – review & editing, Conceptualization. **Uwe Klemm:** Investigation. **Azeem Mohammed:** Investigation. **David Wiesner:** Software. **Mara Saccomano:** Investigation. **Monica Tost:** Investigation. **Annette Feuchtinger:** Resources. **Kanuj Mishra:** Writing – review & editing, Writing – original draft, Investigation. **Oliver Bruns:** Writing – review & editing. **Arie Geerlof:** Investigation. **Vasilis Ntziachristos:** Writing – review & editing. **Andre C. Stiel:** Writing – review & editing, Writing – original draft, Conceptualization.

Declaration of competing interest

The authors declare the following financial interests/personal relationships which may be considered as potential competing interests:

Andre C. Stiel reports financial support was provided by Deutsche Forschungsgemeinschaft. Azeem Mohammed reports financial support was provided by Deutsche Forschungsgemeinschaft. Mariia Stankevych reports financial support was provided by Deutsche Forschungsgemeinschaft. Andre C. Stiel reports financial support was provided by European Research Council. Vasilis Ntziachristos reports a relationship with iThera Medical GmbH that includes: equity or stocks. If there are other authors, they declare that they have no known competing financial interests or personal relationships that could have appeared to influence the work reported in this paper.

Funding statement

M.S., A.M., and A.C.S. acknowledge funding by the Deutsche Forschungsgemeinschaft (STI-656/5-1 and STI-656/6-1). D.W. and A.C.S. acknowledge funding from the European Research Council (ERC) under the European Union's Horizon 2020 research and innovation programme under Grant Agreement No. 101002646 ('Switch2See').

Data availability

The raw/processed data required to reproduce these findings cannot be shared at this time due to technical or time limitations.

Acknowledgments

We acknowledge the technical support of the Flow Cytometry Core Facility and Birgit Rathkolb from the German Mouse Clinic at Helmholtz Munich. We thank Mateusz Strzelecki for his help with Flow Cytometry. We thank Klaudia Winkler for technical support. We thank Dr. Serene Lee for her attentive reading and improvements to the manuscript.

Supplementary materials

Supplementary material associated with this article can be found, in the online version, at doi:10.1016/j.actbio.2025.02.002.

References

[1] V. Ntziachristos, Going deeper than microscopy: the optical imaging frontier in biology, Nat. Methods 7 (8) (2010), 603–14.
[2] L.V. Wang, S. Hu, Photoacoustic tomography: in vivo imaging from organelles to organs, Science 335 (6075) (2012), 1458–62.
[3] I. Steinberg, D.M. Huland, O. Vermesh, H.E. Frostig, W.S. Tummers, S.S. Gambhir, Photoacoustic clinical imaging, Photoacoustics 14 (2019) 77–98.
[4] J. Aguirre, M. Schwarz, N. Garzorz, M. Omar, A. Buehler, K. Eyerich, V. Ntziachristos, Precision assessment of label-free psoriasis biomarkers with ultra-broadband optoacoustic mesoscopy, Nat. Biomed. Eng. 1 (5) (2017), 0068–0068.
[5] J. Reber, M. Willershauser, A. Karlas, K. Paul-Yuan, G. Diot, D. Franz, T. Fromme, S.V. Ovsepian, N. Beziere, E. Dubikovskaya, D.C. Karampinos, C. Holzapfel, H. Hauner, M. Klingenspor, V. Ntziachristos, Non-invasive measurement of brown fat metabolism based on optoacoustic imaging of hemoglobin gradients, Cell Metab. 27 (3) (2018) 689–701. .e4.
[6] F. Knieling, C. Neufert, A. Hartmann, J. Claussen, A. Urich, C. Egger, M. Vetter, S. Fischer, L. Pfeifer, A. Hagel, C. Kielisch, R.S. Gortz, D. Wildner, M. Engel, J. Rother, W. Uter, J. Siebler, R. Atreya, W. Rascher, D. Strobel, M.F. Neurath, M. J. Waldner, Multispectral optoacoustic tomography for assessment of Crohn's disease activity, N. Engl. J. Med. 376 (13) (2017) 1292–1294.
[7] A.P. Regensburger, L.M. Fonteyne, J. Jungert, A.L. Wagner, T. Gerhalter, A. M. Nagel, R. Heiss, F. Flenkenthaler, M. Qurashi, M.F. Neurath, N. Klymiuk, E. Kemter, T. Frohlich, M. Uder, J. Woelfle, W. Rascher, R. Trollmann, E. Wolf, M. J. Waldner, F. Knieling, Detection of collagens by multispectral optoacoustic tomography as an imaging biomarker for Duchenne muscular dystrophy, Nat. Med. 25 (12) (2019), 1905–1915.
[8] Y. Liu, P. Bhattarai, Z. Dai, X. Chen, Photothermal therapy and photoacoustic imaging: via nanotheranostics in fighting cancer, Chem. Soc. Rev. (2019).
[9] J. Yao, L. Wang, J.M. Yang, K.I. Maslov, T.T. Wong, L. Li, C.H. Huang, J. Zou, L. V. Wang, High-speed label-free functional photoacoustic microscopy of mouse brain in action, Nat. Methods 12 (5) (2015), 407–10.

[10] I. Stoffels, S. Morscher, I. Helfrich, U. Hillen, J. Leyh, N.C. Burton, T.C. Sardella, J. Claussen, T.D. Poeppel, H.S. Bachmann, A. Roesch, K. Griewank, D. Schadendorf, M. Gunzer, J. Klode, Metastatic status of sentinel lymph nodes in melanoma determined noninvasively with multispectral optoacoustic imaging, Sci. Transl. Med. 7 (317) (2015) 317ra199.
[11] J. Brunker, J. Yao, J. Laufer, S.E. Bohndiek, Photoacoustic imaging using genetically encoded reporters: a review, J. Biomed. Opt. 22 (7) (2017), 70901–70901.
[12] V. Gujrati, A. Mishra, V. Ntziachristos, Molecular imaging probes for multi-spectral optoacoustic tomography, Chem. Commun. 53 (34) (2017) 4653–4672.
[13] J. Weber, P.C. Beard, S.E. Bohndiek, Contrast agents for molecular photoacoustic imaging, Nat. Methods 13 (8) (2016), 639–50.
[14] N. Liu, K. Mishra, A.C. Stiel, V. Gujrati, V. Ntziachristos, The sound of drug delivery: optoacoustic imaging in pharmacology, Adv. Drug Deliv. Rev. 189 (2022) 114506.
[15] E.I. Galanzha, Y.A. Menyaev, A.C. Yadem, M. Sarimollaoglu, M.A. Juratli, D. A. Nedosekin, S.R. Foster, A. Jamshidi-Parsian, E.R. Siegel, I. Makhoul, L. F. Hutchins, J.Y. Suen, V.P. Zharov, In vivo liquid biopsy using cytophone platform for photoacoustic detection of circulating tumor cells in patients with melanoma, Sci. Transl. Med. 11 (496) (2019).
[16] I. Weidenfeld, C. Zakian, P. Duewell, A. Chmyrov, U. Klemm, J. Aguirre, V. Ntziachristos, A.C. Stiel, Homogentisic acid-derived pigment as a biocompatible label for optoacoustic imaging of macrophages, Nat. Commun. 10 (1) (2019) 5056.
[17] A.P. Jathoul, J. Laufer, O. Ogunlade, B. Treeby, B. Cox, E. Zhang, P. Johnson, A. R. Pizzey, B. Philip, T. Marafioti, M.F. Lythgoe, R.B. Pedley, M.A. Pule, P. Beard, Deep in vivo photoacoustic imaging of mammalian tissues using a tyrosinase-based genetic reporter, Nat. Photonics 9 (4) (2015) 239–246.
[18] A. de la Zerda, S. Bodapati, R. Teed, S.Y. May, S.M. Tabakman, Z. Liu, B.T. Khuri-Yakub, X. Chen, H. Dai, S.S. Gambhir, Family of enhanced photoacoustic imaging agents for high-sensitivity and multiplexing studies in living mice, ACS Nano 6 (6) (2012), 4694–701.
[19] C.W. Kimbrough, A. Khanal, M. Zeiderman, B.R. Khanal, N.C. Burton, K. M. McMasters, S.M. Vickers, W.E. Grizzle, L.R. McNally, Targeting acidity in pancreatic adenocarcinoma: multispectral optoacoustic tomography detects pH-low insertion peptide probes in vivo, Clin. Cancer Res. 21 (20) (2015), 4576–85.
[20] A.C. Stiel, V. Ntziachristos, Controlling the sound of light: photoswitching optoacoustic imaging, Nat. Methods 21 (11) (2024) 1996–2007.
[21] W. Choi, B. Park, S. Choi, D. Oh, J. Kim, C. Kim, Recent advances in contrast-enhanced photoacoustic imaging: overcoming the physical and practical challenges, Chem. Rev. 123 (11) (2023) 7379–7419.
[22] K. Mishra, J.P. Fuenzalida-Werner, V. Ntziachristos, A.C. Stiel, Photocontrollable proteins for optoacoustic imaging, Anal. Chem. 91 (9) (2019) 5470–5477.
[23] L. Li, A.A. Shemetov, M. Baloban, P. Hu, L. Zhu, D.M. Shcherbakova, R. Zhang, J. Shi, J. Yao, L.V. Wang, V.V. Verkhusha, Small near-infrared photochromic protein for photoacoustic multi-contrast imaging and detection of protein interactions in vivo, Nat. Commun. 9 (1) (2018) 2734.
[24] J. Yao, A.A. Kaberniuk, L. Li, D.M. Shcherbakova, R. Zhang, L. Wang, G. Li, V. V. Verkhusha, L.V. Wang, Multiscale photoacoustic tomography using reversibly switchable bacterial phytochrome as a near-infrared photochromic probe, Nat. Methods 13 (1) (2016) 67–73.
[25] K. Mishra, M. Stankevych, J.P. Fuenzalida-Werner, S. Grassmann, V. Gujrati, Y. Huang, U. Klemm, V.R. Buchholz, V. Ntziachristos, A.C. Stiel, Multiplexed whole-animal imaging with reversibly switchable optoacoustic proteins, Sci. Adv. 6 (24) (2020) eaaz6293.
[26] J. Märk, H. Dortay, A. Wagener, E. Zhang, J. Buchmann, C. Grötzinger, T. Friedrich, J. Laufer, Dual-wavelength 3D photoacoustic imaging of mammalian cells using a photoswitchable phytochrome reporter protein, Commun. Phys. 1 (1) (2018), 3–3.
[27] L.A. Kasatkina, C. Ma, M.E. Matlashov, T. Vu, M. Li, A.A. Kaberniuk, J. Yao, V. V. Verkhusha, Optogenetic manipulation and photoacoustic imaging using a near-infrared transgenic mouse model, Nat. Commun. 13 (1) (2022) 2813.
[28] L. Nie, X. Chen, Structural and functional photoacoustic molecular tomography aided by emerging contrast agents, Chem. Soc. Rev. 43 (20) (2014), 7132–70.
[29] M.A. Dobrovolskaia, D.R. Germolec, J.L. Weaver, Evaluation of nanoparticle immunotoxicity, Nat. Nanotechnol. 4 (7) (2009), 411–4.
[30] T. Fukaminato, S. Ishida, R. Métivier, Photochromic fluorophores at the molecular and nanoparticle levels: fundamentals and applications of diarylethenes, NPG Asia Mater. 10 (9) (2018) 859–881.
[31] M. Irie, T. Fukaminato, K. Matsuda, S. Kobatake, Photochromism of diarylethene molecules and crystals: memories, switches, and actuators, Chem. Rev. 114 (24) (2014), 12174–277.
[32] G.T. Dempsey, M. Bates, W.E. Kowtoniuk, D.R. Liu, R.Y. Tsien, X. Zhuang, Photoswitching mechanism of cyanine dyes, J. Am. Chem. Soc. 131 (51) (2009), 18192–3.
[33] L.N. Lameijer, S. Budzak, N.A. Simeth, M.J. Hansen, B.L. Feringa, D. Jacquemin, W. Szymanski, General principles for the design of visible-light-responsive photoswitches: tetra-ortho-chloro-azobenzenes, Angew. Chem. Int. Ed. Engl. 59 (48) (2020) 21663–21670.
[34] Y. Yang, R.P. Hughes, I. Aprahamian, Near-infrared light activated azo-BF2 switches, J. Am. Chem. Soc. 136 (38) (2014), 13190–3.
[35] A.A. Beharry, O. Sadovski, G.A. Woolley, Azobenzene photoswitching without ultraviolet light, J. Am. Chem. Soc. 133 (49) (2011), 19684–7.
[36] C. Liu, X. Zheng, T. Dai, H. Wang, X. Chen, B. Chen, T. Sun, F. Wang, S. Chu, J. Rao, Reversibly photoswitching upconversion nanoparticles for super-sensitive photoacoustic molecular imaging, Angew. Chem. Int. Ed. Engl. 61 (19) (2022) e202116802.
[37] D.M. Shcherbakova, M. Baloban, S. Pletnev, V.N. Malashkevich, H. Xiao, Z. Dauter, V.V. Verkhusha, Molecular basis of spectral diversity in near-infrared phytochrome-based fluorescent proteins, Chem. Biol. 22 (11) (2015) 1540–1551.
[38] V. Schellenberger, C.W. Wang, N.C. Geething, B.J. Spink, A. Campbell, W. To, M. D. Scholle, Y. Yin, Y. Yao, O. Bogin, J.L. Cleland, J. Silverman, W.P. Stemmer, A recombinant polypeptide extends the in vivo half-life of peptides and proteins in a tunable manner, Nat. Biotechnol. 27 (12) (2009), 1186–90.
[39] B.A. Konkle, A.D. Shapiro, D.V. Quon, J.M. Staber, R. Kulkarni, M.V. Ragni, E. S. Chhabra, S. Poloskey, K. Rice, S. Katragadda, J. Fruebis, C.C. Benson, BIVV001 Fusion protein as factor VIII replacement therapy for hemophilia A, N. Engl. J. Med. 383 (11) (2020) 1018–1027.
[40] A. Haeckel, F. Appler, L. Figge, H. Kratz, M. Lukas, R. Michel, J. Schnorr, M. Zille, B. Hamm, E. Schellenberger, XTEN-annexin A5: XTEN allows complete expression of long-circulating protein-based imaging probes as recombinant alternative to PEGylation, J. Nucl. Med. 55 (3) (2014), 508–14.
[41] A. Nomani, G. Li, S. Yousefi, S. Wu, O.M. Malekshah, S.K. Nikkhoi, M. Pourfathi, R. Rizi, A. Hatefi, Gadolinium-labeled affibody-XTEN recombinant vector for detection of HER2+ lesions of ovarian cancer lung metastasis using quantitative MRI, J. Control Release 337 (2021) 132–143.
[42] F. Brandl, S. Busslinger, U. Zangemeister-Wittke, A. Pluckthun, Optimizing the anti-tumor efficacy of protein-drug conjugates by engineering the molecular size and half-life, J. Control Release 327 (2020) 186–197.
[43] M.D. Onsum, E. Geretti, V. Paragas, A.J. Kudla, S.P. Moulis, L. Luus, T.J. Wickham, C.F. McDonagh, G. MacBeath, B.S. Hendriks, Single-cell quantitative HER2 measurement identifies heterogeneity and distinct subgroups within traditionally defined HER2-positive patients, Am. J. Pathol. 183 (5) (2013) 1446–1460.
[44] A. Nocito, F. Dahm, W. Jochum, J.H. Jang, P. Georgiev, M. Bader, R. Graf, P. A. Clavien, Serotonin regulates macrophage-mediated angiogenesis in a mouse model of colon cancer allografts, Cancer Res. 68 (13) (2008), 5152–8.
[45] G. Shechter, C. Ozturk, J.R. Resar, E.R. McVeigh, Respiratory motion of the heart from free breathing coronary angiograms, IEEE Trans. Med. ImAging 23 (8) (2004), 1046–56.
[46] J.P. Thirion, Image matching as a diffusion process: an analogy with Maxwell's demons, Med. Image Anal. 2 (3) (1998), 243–60.
[47] L.V. Wang, H.-i. Wu, Biomedical Optics: Principles and Imaging, 1st editio ed., Wiley-Interscience, 2007.
[48] J.D. Malley, J. Kruppa, A. Dasgupta, K.G. Malley, A. Ziegler, Probability machines: consistent probability estimation using nonparametric learning machines, Methods Inf. Med. 51 (1) (2012) 74–81.
[49] A. Jimenez-Banzo, S. Nonell, J. Hofkens, C. Flors, Singlet oxygen photosensitization by EGFP and its chromophore HBDI, Biophys. J. 94 (1) (2008), 168–72.
[50] V.N. Podust, S. Balan, B.C. Sim, M.P. Coyle, U. Ernst, R.T. Peters, V. Schellenberger, Extension of in vivo half-life of biologically active molecules by XTEN protein polymers, J. Control Release 240 (2016) 52–66.
[51] E. Seth Chhabra, N. Moore, C. Furcht, A.M. Holthaus, J. Liu, T. Liu, V. Schellenberger, J. Kulman, J. Salas, R. Peters, Evaluation of enhanced in vitro plasma stability of a novel long acting recombinant FVIIIFc-VWF-XTEN fusion protein, Blood 126 (23) (2015) 2279.
[52] X. Wang, G. Ku, M.A. Wegiel, D.J. Bornhop, G. Stoica, L.V. Wang, Noninvasive photoacoustic angiography of animal brains in vivo with near-infrared light and an optical contrast agent, Opt. Lett. 29 (7) (2004), 730–2.
[53] C. Kim, K.H. Song, F. Gao, L.V. Wang, Sentinel lymph nodes and lymphatic vessels: noninvasive dual-modality in vivo mapping by using indocyanine green in rats–volumetric spectroscopic photoacoustic imaging and planar fluorescence imaging, Radiology 255 (2) (2010), 442–50.
[54] W.S. Tummers, S.E. Miller, N.T. Teraphongphom, A. Gomez, I. Steinberg, D. M. Huland, S. Hong, S.R. Kothapalli, A. Hasan, R. Ertsey, B.A. Bonsing, A. L. Vahrmeijer, R.J. Swijnenburg, T.A. Longacre, G.A. Fisher, S.S. Gambhir, G. A. Poultsides, E.L. Rosenthal, Intraoperative pancreatic cancer detection using tumor-specific multimodality molecular imaging, Ann. Surg. Oncol. 25 (7) (2018) 1880–1888.
[55] P.C. Li, C.R. Wang, D.B. Shieh, C.W. Wei, C.K. Liao, C. Poe, S. Jhan, A.A. Ding, Y. N. Wu, In vivo photoacoustic molecular imaging with simultaneous multiple selective targeting using antibody-conjugated gold nanorods, Opt. Express. 16 (23) (2008), 18605–15.
[56] M. Stankevych, K. Mishra, V. Ntziachristos, A.C. Stiel, A practical guide to photoswitching optoacoustics tomography, Meth. Enzymol. (2021) 365–383.
[57] J. Yao, L.V. Wang, Sensitivity of photoacoustic microscopy, Photoacoustics 2 (2) (2014) 87–101.
[58] A. Orlova, M. Magnusson, T.L. Eriksson, M. Nilsson, B. Larsson, I. Hoiden-Guthenberg, C. Widstrom, J. Carlsson, V. Tolmachev, S. Stahl, F.Y. Nilsson, Tumor imaging using a picomolar affinity HER2 binding affibody molecule, Cancer Res. 66 (8) (2006), 4339–48.
[59] S. Stahl, T. Graslund, A. Eriksson Karlstrom, F.Y. Frejd, P.A. Nygren, J. Lofblom, Affibody molecules in biotechnological and medical applications, Trends Biotechnol. 35 (8) (2017) 691–712.
[60] H. Liu, M. Wang, F. Ji, Y. Jiang, M. Yang, Mini review of photoacoustic clinical imaging: a noninvasive tool for disease diagnosis and treatment evaluation, J. Biomed. Opt. 29 (Suppl 1) (2024) S11522.
[61] M.M. Deken, D.L. Bos, W. Tummers, T.L. March, C.J.H. van de Velde, M. Rijpkema, A.L. Vahrmeijer, Multimodal image-guided surgery of HER2-positive breast cancer using [(111)In]In-DTPA-trastuzumab-IRDye800CW in an orthotopic breast tumor model, EJNMMI. Res. 9 (1) (2019) 98.

[62] H. Wang, D. Jia, D. Yuan, X. Yin, F. Yuan, F. Wang, W. Shi, H. Li, L.M. Zhu, Q. Fan, Dimeric Her2-specific affibody mediated cisplatin-loaded nanoparticles for tumor enhanced chemo-radiotherapy, J. Nanobiotechnology 19 (1) (2021) 138.
[63] S.E. Alters, B. McLaughlin, B. Spink, T. Lachinyan, C.W. Wang, V. Podust, V. Schellenberger, W.P. Stemmer, GLP2-2G-XTEN: a pharmaceutical protein with improved serum half-life and efficacy in a rat Crohn's disease model, PLoS One 7 (11) (2012) e50630.
[64] E. Seth Chhabra, T. Liu, J. Kulman, S. Patarroyo-White, B. Yang, Q. Lu, D. Drager, N. Moore, J. Liu, A.M. Holthaus, J.M. Sommer, A. Ismail, D. Rabinovich, Z. Liu, A. van der Flier, A. Goodman, C. Furcht, M. Tie, T. Carlage, R. Mauldin, T. M. Dobrowsky, Z. Liu, O. Mercury, L. Zhu, B. Mei, V. Schellenberger, H. Jiang, G. F. Pierce, J. Salas, R. Peters, BIVV001, a new class of factor VIII replacement for hemophilia A that is independent of von Willebrand factor in primates and mice, Blood 135 (17) (2020) 1484–1496.
[65] A.B.E. Attia, G. Balasundaram, M. Moothanchery, U.S. Dinish, R. Bi, V. Ntziachristos, M. Olivo, A review of clinical photoacoustic imaging: current and future trends, Photoacoustics 16 (July) (2019) 100144.
[66] H. Guo, Y. Li, W. Qi, L. Xi, Photoacoustic endoscopy: a progress review, J. Biophotonics 13 (12) (2020) e202000217.
[67] S. Na, J.J. Russin, L. Lin, X. Yuan, P. Hu, K.B. Jann, L. Yan, K. Maslov, J. Shi, D. J. Wang, C.Y. Liu, L.V. Wang, Massively parallel functional photoacoustic computed tomography of the human brain, Nat. Biomed. Eng. 6 (5) (2022) 584–592.
[68] C. Lutzweiler, R. Meier, E. Rummeny, V. Ntziachristos, D. Razansky, Real-time optoacoustic tomography of indocyanine green perfusion and oxygenation parameters in human finger vasculature, Opt. Lett. 39 (14) (2014), 4061–4.
[69] W. Shan, R. Chen, Q. Zhang, J. Zhao, B. Chen, X. Zhou, S. Ye, S. Bi, L. Nie, L. Ren, Improved stable indocyanine green (ICG)-mediated cancer optotheranostics with naturalized hepatitis B core particles, Adv. Mater. 30 (28) (2018) e1707567.
[70] K. Okumura, K. Yoshida, K. Yoshioka, S. Aki, N. Yoneda, D. Inoue, A. Kitao, T. Ogi, K. Kozaka, T. Minami, W. Koda, S. Kobayashi, Y. Takuwa, T. Gabata, Photoacoustic imaging of tumour vascular permeability with indocyanine green in a mouse model, Eur. Radiol. Exp. 2 (1) (2018) 5.
[71] S. Zhang, L. Qi, X. Li, J. Liu, S. Huang, J. Wu, R. Liu, Y. Feng, Q. Feng, W. Chen, Photoacoustic imaging of living mice enhanced with a low-cost contrast agent, Biomed. Opt. Express. 10 (11) (2019) 5744–5754.
[72] Z. Gao, G. Li, X. Li, J. Zhou, X. Duan, J. Chen, B.P. Joshi, R. Kuick, B. Khoury, D. G. Thomas, T. Fields, M.S. Sabel, H.D. Appelman, Q. Zhou, H. Li, K. Kozloff, T. D. Wang, In vivo near-infrared imaging of ErbB2 expressing breast tumors with dual-axes confocal endomicroscopy using a targeted peptide, Sci. Rep. 7 (1) (2017) 14404.
[73] R. Su, A.V. Liopo, H.-P. Brecht, S.A. Ermilov, A.A. Oraevsky, Gold nanorod distribution in mouse tissues after intravenous injection monitored with optoacoustic tomography, Photons Plus Ultrasound: Imaging Sens. 7899 (March 2017) (2011), 201178994B–78994B.
[74] J.V. Jokerst, A.J. Cole, D. Van de Sompel, S.S. Gambhir, Gold nanorods for ovarian cancer detection with photoacoustic imaging and resection guidance via Raman imaging in living mice, ACS Nano 6 (11) (2012), 10366–77.
[75] Q. Fu, R. Zhu, J. Song, H. Yang, X. Chen, Photoacoustic imaging: contrast agents and their biomedical applications, Adv. Mater. 31 (2019) 1–31.
[76] M. Seeger, A. Stylogiannis, L. Prade, S. Glasl, V. Ntziachristos, Overdriven laser diode optoacoustic microscopy, Sci. Rep. 13 (1) (2023) 19542.
[77] P.K. Upputuri, M. Pramanik, Fast photoacoustic imaging systems using pulsed laser diodes: a review, Biomed. Eng. Lett. 8 (2) (2018) 167–181.
[78] S. Ahmadpour, S.J. Hosseinimehr, PASylation as a powerful technology for improving the pharmacokinetic properties of biopharmaceuticals, Curr. Drug Deliv. 15 (3) (2018) 331–341.
[79] F. Khodabakhsh, M. Salimian, M.H. Hedayati, R. Ahangari Cohan, D. Norouzian, Challenges and advancements in the pharmacokinetic enhancement of therapeutic proteins, Prep. Biochem. Biotechnol. 51 (6) (2021) 519–529.
[80] A. Richter, K. Knorr, M. Schlapschy, S. Robu, V. Morath, C. Mendler, H.Y. Yen, K. Steiger, M. Kiechle, W. Weber, A. Skerra, M. Schwaiger, First in-human medical imaging with a PASylated (89)Zr-labeled anti-HER2 fab-fragment in a patient with metastatic breast cancer, Nucl. Med. Mol. Imaging 54 (2) (2020) 114–119.